Biomaterials and Biosystems 13 (2024) 100086

Contents lists available at ScienceDirect

Biomaterials and Biosystems

journal homepage: www.elsevier.com/locate/bbiosy

3D printed bioabsorbable composite scaffolds of poly (lactic acid)-tricalcium phosphate-ceria with osteogenic property for bone regeneration

Samarah V. Harb [a,b,*], Elayaraja Kolanthai [b], Abinaya S. Pugazhendhi [c], Cesar A.G. Beatrice [a], Leonardo A. Pinto [d], Craig J. Neal [b], Eduardo H. Backes [a], Ana C.C. Nunes [e], Heloisa S. Selistre-de-Araújo [e], Lidiane C. Costa [a], Melanie J. Coathup [c], Sudipta Seal [b,c], Luiz A. Pessan [a]

[a] Department of Materials Engineering (DEMa), Federal University of Sao Carlos (UFSCar), São Carlos, SP, Brazil
[b] Advanced Materials Processing and Analysis Center, Department of Materials Science and Engineering, University of Central Florida, Orlando, FL, USA
[c] Biionix Cluster, College of Medicine, University of Central Florida, Orlando, FL, USA
[d] Graduate Program in Materials Science and Engineering, Department of Materials Engineering (DEMa), Federal University of São Carlos (UFSCar), São Carlos, SP, Brazil
[e] Department of Physiological Sciences, Federal University of São Carlos (UFSCar), São Carlos, SP, Brazil

ARTICLE INFO

Keywords:
Bone tissue engineering
Polymer-matrix composites
Ceria nanoparticle
Additive manufacturing
Biomaterial

ABSTRACT

The fabrication of customized implants by additive manufacturing has allowed continued development of the personalized medicine field. Herein, a 3D-printed bioabsorbable poly (lactic acid) (PLA)- β-tricalcium phosphate (TCP) (10 wt %) composite has been modified with CeO_2 nanoparticles (CeNPs) (1, 5 and 10 wt %) for bone repair. The filaments were prepared by melt extrusion and used to print porous scaffolds. The nanocomposite scaffolds possessed precise structure with fine print resolution, a homogenous distribution of TCP and CeNP components, and mechanical properties appropriate for bone tissue engineering applications. Cell proliferation assays using osteoblast cultures confirmed the cytocompatibility of the composites. In addition, the presence of CeNPs enhanced the proliferation and differentiation of mesenchymal stem cells; thereby, increasing alkaline phosphatase (ALP) activity, calcium deposition and bone-related gene expression. Results from this study have shown that the 3D printed PLA-TCP-10%CeO_2 composite scaffold could be used as an alternative polymeric implant for bone tissue engineering applications: avoiding additional/revision surgeries and accelerating the regenerative process.

1. Introduction

The increasing life expectancy of the world population has led to a growing need for orthopedic, bone repair procedures to address fractures, osteoporosis, and tumors for the prowing number of advanced-age patients [1,2]. Among these procedures are immobilization, surgical procedures for prosthesis incorporation or fixation of bone fragments with plates and screws, and bone grafting. For prosthetic and fixation devices, metallic materials such as stainless steel and titanium alloys are typically employed. However, these materials present several disadvantages, including stress shielding, the release of toxic ions to the body, and slow osseointegration [1,3]. For bone grafts, the gold standard is the use of autogenous bone, which is limited as a primary therapeutic option due to the finite source availibility, sequelae at the graft donor site (pain, sensitivity changes and scars), and the necessity of additional surgical procedures [4]. Currently, intense focus has been devoted to the development of 3D printed biodegradable scaffolds that act as temporary reparative materials for bone regeneration [5,6]. These scaffolds degrade into the body producing non-toxic species as the tissue is completely regenerated; thereby, avoiding the need for further surgical interventions and chronic pain at the repaired site. The use of additive manufacturing, in the production of such bone repair scaffolds, allows

* Corresponding author at: Department of Materials Engineering (DEMa), Federal University of São Carlos (UFSCar), Rodovia Washington Luis, km 235, São Carlos, SP 13565-970, Brazil.
E-mail address: samarah@estudante.ufscar.br (S.V. Harb).

https://doi.org/10.1016/j.bbiosy.2023.100086
Received 8 September 2023; Received in revised form 28 November 2023; Accepted 17 December 2023
Available online 18 December 2023

for control of the scaffold structure and, consequently, the possibility for individual customization [7,8].

Poly (lactic acid) (PLA) has stood out among the various materials explored for bone repair in terms of therapeutic performance and utility. PLA is produced with a controllable structure from a renewable source; as well as being bioabsorbable, biocompatible and presenting mechanical behavior appropriate for bone tissue engineering [9–11]. In addition, the easy processability of PLA facilitates its use in additive manufacturing. However, the major drawback of PLA application in the biomedical field is its lack of bioactivity, which delays the adhesion and proliferation of cells. The incorporation of calcium phosphates, such as β-tricalcium phosphate (TCP) and hydroxyapatite (HA), into PLA matrices has been the most exploited strategy to impart bioactivity [12–17]. Backes and co-workers have incorporated different concentrations of HA and TCP into the PLA matrix and demonstrated that the PLA-10wt %TCP composite presents adequate properties for bone scaffold fabrication in terms of rheology, biocompatibility and mechanical resistance [12,14]. Despite the predominance in research literature and success of this strategy in improving bioactivity, alternative materials are being evaluated which may further enhance bone regeneration, such as the use of cerium oxide.

Cerium oxide nanoparticles (CeNPs) have recently been highlighted in research literature due to their positive effect on bone cell proliferation [18,19], stem cells differentiation [18,19], stimulation of vascularization [20], antioxidant activity [19,21,22] and antimicrobial properties [23–25]. In recent years, cerium (oxide) has been incorporated into bio-glasses (BG) to improve the function of osteoblasts [26–28]. Lu et al. [18] incorporated BG microparticles containing cerium oxide nanoparticles in a chitosan matrix through the lyophilization technique. *In vitro* and *in vivo* results confirmed that the presence of cerium oxide accelerated mesenchymal stem cell differentiation, collagen deposition, and bone regeneration as compared to scaffolds using only chitosan-BG [18]. Nanoparticles of CeO_2 were also added in a poly (lactic-co-glycolic acid) (PLGA) matrix by mixing the cerium oxide powder with polymeric solutions in dichloromethane (solvent casting) and subsequently obtaining scaffolds in pre-stamped molds [29]. The authors observed that PLGA-CeO_2 scaffolds had a greater ability to promote the growth of mesenchymal stem cells, compared to pure PLGA [29].

In addition to stimulating cell proliferation and differentiation, cerium oxide nanoparticles demonstrated efficacy in enhancing vascularization by activating calcium channels in mesenchymal stem cells [20]. Xiang et al. [20] have improved blood vessel distribution in bone grafts by impregnating cancellous bone scaffolds with poly (L-lactide) and CeNPs. Furthermore, cerium oxide may also provide anti-inflammatory activity due to its antioxidant property, mitigating inflammatory reactions induced by implants [19]. Using a plasma spray technique, Li and coauthors incorporated 10 and 30 % CeO_2 in HA coatings on Ti6Al4V alloy substrates to promote osteogenic responses and reduce inflammatory reactions [19]. The addition of CeO_2 to the coatings conferred anti-inflammatory properties and resulted in improved osteogenic behaviors of mesenchymal stem cells in terms of cell proliferation, alkaline phosphatase (ALP) activity and formation of mineralized nodules, compared to pure HA [19].

The aim of this study was to develop porous, biodegradable, and 3D printable PLA/TCP/CeNPs scaffolds to promote bone tissue regeneration. Our research aimed to leverage additive manufacturing for the production of personalized medicine scaffolds, offering tailored and patient-specific solutions. We have taken advantage of the extrusion process to manufacture homogeneous composite filaments that can be directly printed into bioactive constructs. The possibility of fabricating and storing the filaments with a ready-to-use composition reduces costs and accelerates the time for implant fabrication. We hypothesized that the presence of CeNPs, especially in higher loads, would promote cell proliferation and induce osteogenic behavior. The incorporation of CeNPs (1, 5, and 10 wt %) into a PLA/TCP (fixed composition: 90 wt %/10 wt %) matrix during the extrusion process for filament fabrication led to the formation of homogenous nanocomposites with reproducible properties. Subsequent use of additive manufacturing to prepare the scaffold allowed for a controllable porous structure. We have analyzed the structural, mechanical, rheological, and thermal character of all control and test samples. Furthermore, cellular responses towards the produced 3D scaffolds were evaluated as osteoblast cell proliferation and stem cell osteogenic differentiation for *in vitro* conditions.

2. Materials and methods

2.1. Materials

PLA 2003D was purchased from NatureWorks in the form of pellets and was cryogenically ground using a Mikro-Bantam® hammer mill (Hosokawa Micron Powder Systems). The PLA powder was dried in a vacuum oven at 60 °C for 1 h and 80 °C for 4 h and kept in a vacuum desiccator until used. TCP (nanoXIM-TCP200, >95 %, CAS#: 7758-87-4) was acquired from FLUIDINOVA. The white TCP powder consists of 5 μm nanostructured microparticles and was previously sintered at 1000 °C for 1 h using a heating rate of 10 °C min^{-1}. CeO_2 nanoparticles (CeNPs, 99.5 % min, 15-30 nm, #44960, CAS#: 1306-38-3) were purchased from Alfa Aesar.

2.2. Filament fabrication

Before extrusion, the powder components (PLA, TCP, and CeNPs) were dried, weighed and placed in plastic bags for homogenization (Table S1). Filaments were produced *via* extrusion. An extrusion machine for filament fabrication operates by feeding the raw material into a heated barrel, where it is melted. The molten material is then extruded through a nozzle, creating a continuous filament that is cooled in a water bath, allowed to solidify, and subsequently wound onto a spool for use in 3D printing. A co-rotating twin-screw extruder (MT19TC, B&P Process Equipment and Systems) with a diameter of 19 mm and L/D of 25 was employed to prepare the filaments with 1.75 ± 0.10 mm thickness, using a screw speed of 30 rpm, temperature of 175 °C, and a feed rate of 1 kg h^{-1} (Scheme 1).

2.3. Scaffold 3D-printing

The scaffolds were designed using the Solidworks® software and produced by fused filament fabrication (FFF) (Scheme 1). Individual samples were cylindrical, 8 mm in diameter, comprised of 10 layers (3.6 mm of height), with 300 μm between filaments (pore size), and a deposition pattern of 0-90°. The drawing was sliced by the Slic3r software and printed with the Repetier-Host software, which allows control of the Sethi3D S3 printer. For printing the scaffolds, the following configuration was used: a nozzle with a diameter of 400 μm, bed temperature of 55 °C, first layer printing speed of 10 mm s^{-1}, and printing speed of 20 mm s^{-1} for subsequent layers. For pure PLA and PLA-TCP scaffolds, a printing temperature of 175 °C was used, while scaffolds containing CeNPs were printed at 165 °C.

2.4. Characterization

2.4.1. Morphology and composition

The commercial CeNPs were dispersed in ethanol and deposited on a carbon-coated copper grid for TEM measurements in a FEI Tecnai G^2 F20 microscope operated at 200 kV. The CeNPs were also characterized by zeta potential measurements using a Zetasizer nano series equipment (Malvern Instruments) with a disposable folded capillary cell containing the 5 mM CeNPs dispersed in water.

The CeNPs powder, TCP powder, PLA scaffold and PLA-TCP-10% CeO_2 scaffold were analyzed by X-ray diffraction (XRD) and X-ray photoelectron spectroscopy (XPS). All samples were characterized

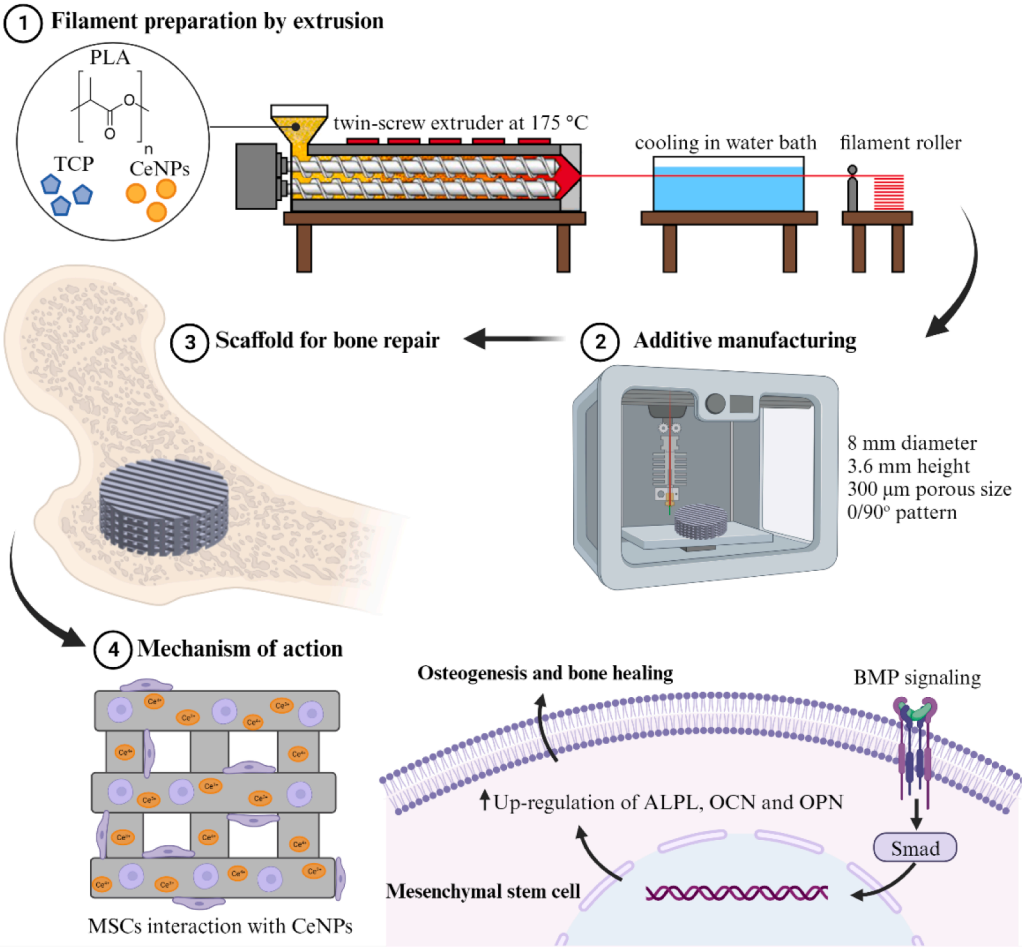

Scheme 1. Experimental procedure to obtain PLA-TCP-CeO_2 scaffolds and their potential osteogenic mechanism. PLA, TCP and CeNPs powders are poured into a twin-screw extruder at 175 °C. The filament is extruded with a constant diameter of 1.75 mm, immersed in a water bath for cooling, and collected as a spool. The filament spool is then used to print the scaffolds by additive manufacturing. The interaction of cerium oxide nanoparticles with mesenchymal stem cells activates the Smad-dependent BMP signaling pathway, promoting osteogenesis and bone healing.

without additional preparation or modification. The XRD measurements were performed in an Empyrean system (Malvern Panalytical) equipped with a 1.8 kW copper X-ray tube. XPS was performed using a Thermo Fisher ESCALAB-250 Xi spectrometer, under ultrahigh vacuum (below 8 $\times$ 10^{-10} mbar), monochromatic Al Kα radiation with 300 W (15 kV, 20 mA) operating power, and spot size of 250 µm. XPS data analysis was performed using Thermo *Avantage* software, with the C 1s peak (284.6 eV) considered for binding energy calibration and an *Avantage* 'smart' baseline fitting. Unique chemical states were assigned to fitted peaks through reference to spectra data from Thermo Scientific and/or related published literature.

Scanning electron microscopy (SEM) coupled to energy dispersive X-ray spectroscopy (EDS) (Philips XL-30 FEG and Tescan MIRA FEG) was applied to evaluate the morphology of the scaffolds and the distribution of the additives in the polymeric matrix. Additionally, SEM was performed to visualize osteoblast adhesion on the scaffolds. After 1 day of cell culture, the samples were fixed with 10 % paraformaldehyde for 30 min, dehydrated with graded ethanol solutions (50, 70, 90 and 100 %) and dried at 40 °C under vacuum. Prior to all measurements, a thin layer of gold was deposited on the scaffolds using a Balzers SCD 004 sputter coater equipment.

2.4.2. Thermal and rheological analysis

Differential scanning calorimetry (DSC) and thermogravimetric analysis (TGA) were performed for thermal property characterization. The onset degradation temperature (T_{onset}), the temperature of maximum decomposition (T_{max}) and the percentage of the inorganic compounds in the nanocomposites were obtained by TGA (TA Instruments, model Q50). For TGA analysis, 15 mg of filament was placed in a platinum crucible, and the measurement was performed under a nitrogen flow of 100 mL min^{-1}, with heating up to 750 °C at 10 °C min^{-1}. The crystallization degree (X_c), glass transition temperature (T_g), cold crystallization temperature (T_{cc}), and melting temperature (T_m) were obtained by DSC (TA Instruments, model DSC Q2000). For DSC analysis, 7 mg of filament was placed in an aluminum pan, and the measurement was performed under a nitrogen flow of 50 mL min^{-1}, with heating from 0 °C to 200 °C at 10 °C min^{-1}, followed by cooling from 200 °C to 0 °C and a second heating from 0 °C to 200 °C. The values of T_g, T_{cc} and T_m were determined from the second heating curve, and the crystallization degree (X_c) from the following equation:

$$X_c(\%) = \frac{(\Delta H_m - \Delta H_{cc})}{\Delta H_m^o \varnothing} \times 100 \quad (1)$$

Where ΔH_m is the enthalpy of fusion, ΔH_{cc} is the enthalpy of cold crystallization, ΔH_m^o is the enthalpy of fusion of 100 % crystalline PLA (93.0 J g^{-1} [30]), and ∅ is the weight fraction of PLA in the composites.

Rheological characterization was conducted on filaments in steady and oscillatory states using a stress-controlled rheometer (TA Instruments, AR-G2) with parallel plate geometry (plate diameter of 25.0 mm and distance between plates of 1.0 mm), under a nitrogen atmosphere. Oscillatory state measurements were performed by applying a strain amplitude within the linear viscoelastic regime for each material.

The viscosity measurements at shear rates above 100 s^{-1} were performed in a capillary rheometer (Instron, model 5547) using a die with a diameter of 0.762 mm and an L/D ratio of 32. Rabinowitsch's correction was employed to remove the contribution of the friction between the piston and the barrel. All filaments were analyzed at 165 °C and 175 °C.

2.4.3. Compression testing and wettablity

Mechanical characterization of the materials was performed on the cylindrical scaffolds using a universal testing machine (Instron, model 5569), with a load cell of 500 N. A pre-load of 1 N was applied to the samples, and the samples were tested at a rate of 1.3 mm min^{-1}. The Bluehill 2.15 software was used to acquire the data and extract the values of elastic modulus from the linear region of the stress-strain curves. The mean value of elastic modulus ± standard deviation was obtained from the measurement of five specimens of each composition.

Contact angle measurements were performed in an optical tensiometer (Biolin Scientific, Attension Theta Flex TF3000-Plus). A drop of purified water with 7 μL was dispensed on the scaffold surface and the measurement was performed after 10 s using the OneAttension software. The contact angle (θ) values were obtained from an average of five drops.

2.4.4. Degradation assay

For the degradation experiment, two solutions were used: pure phosphate buffered saline (PBS, Merck) and 0.1667 mg mL^{-1} proteinase K in PBS (5 U mL^{-1}, Merck). First, the scaffolds were vacuum-dried and the dry-weight measured. Afterward, the scaffolds were immersed in PBS (5 mL) and PBS containing proteinase (1 mL) and incubated at 37 °C (N=3). After pre-determined times, the scaffolds were washed with distilled water, dried under vacuum, and weighed. In sequence, fresh solutions were added, and the samples were incubated at 37 °C.

For ICP-MS analysis, samples from each composition of scaffold were immersed in 0.5 mL of osteogenic ingredient containing growth medium and incubated at 37 °C under CO_2 atmosphere for 14 and 28 days. After these time intervals, samples from scaffold-immersed media were collected. Samples were then digested in 35 % HNO_3 (Millipore Sigma) and heated at 65 °C for 48 h before dilution and measurement. ICP-MS measurements were conducted at the University of South Florida (Tampa Bay Plasma Facility, College of Marine Sciences) using a Thermo Element CR High-Resolution instrument. Samples were introduced using a microflow nebulizer (Elemental Scientific PFA μFlow nebulizer) and Glass Expansion Helix cyclonic spray chamber.

2.4.5. Antioxidant activity

The superoxide dismutase (SOD) mimetic activity of the CeNPs was measured using a Dojindo Molecular Technologies SOD assay kit. The kit uses a water-soluble tetrazolium salt, WST-1 (2-(4-iodophenyl)-3-(4-nitrophenyl)-5-(2,4-disulfo-phenyl)-2H-tetrazolium, monosodium salt), which produces a water-soluble formazan dye upon reduction by a superoxide anion. A 1 mM CeNPs solution was prepared in water and the assay was performed following the manufacturer's instructions. After 20 min following enzyme addition, the absorbance was measured at 450 nm on a microplate reader (FLUOstar® Omega, BMG LABTECH). The average values of the samples, measured in triplicate, were used to calculate percentage value measures of SOD activity from derived slope values.

2.4.6. Protein adsorption

The amount of bovine serum albumin (BSA) adsorbed on the scaffolds was quantified by the Pierce™ BCA Protein Assay Kit (Thermo Fisher Scientific). The samples were placed in a 48-well plate, 0.4 mL of a 2 mg mL^{-1} BSA solution (BSA, Sigma-Aldrich) in phosphate-buffered saline (PBS, Merck) was added and the plate was kept inside an incubator at 37 °C for 24 h. The scaffolds were then transferred to a new plate, washed twice with 0.4 mL of PBS, and 0.4 mL of RIPA buffer (Sigma-Aldrich) was used for protein solubilization (10 min in contact and homogenization with pipette). In a 96-well plate, 200 μL of the working reagent was added along with 25 μL of the samples (RIPA + adsorbed proteins) or 25 μL of the prepared calibration standards containing different concentrations of BSA in RIPA. The plate was incubated at 37 °C for 30 min, cooled to room temperature, and absorbance was measured at 562 nm using a spectrophotometer (SpectraMax i3, Molecular Devices). The concentration of protein was determined through a calibration curve using BSA standards.

2.5. Cell studies

2.5.1. Osteoblastic proliferation

Prior to biological assays, the printed scaffolds were immersed in 70 % ethanol for 5 min; then, the scaffolds were dried in lint-free tissue paper (KIMTECH) and irradiated with UV light inside a biological safety cabinet for 60 min (30 min, per side). After sterilization, the scaffolds were placed in a 48-well cell culture plate and washed with 0.4 mL of sterile PBS to remove any possible debris and remaining ethanol.

Pre-osteoblastic mouse cells MC3T3-E4 (ATCC CRL-2593) were cultured in a medium containing 90 %v/v of α-MEM (Gibco) supplemented with 10 % fetal bovine serum (FBS, Vitrocell), in an incubator (series II 3110, Thermo Fisher Scientific) at 37 °C, humidified and containing 5 % CO_2. For cell proliferation assays using Alamar Blue™ Cell Viability Reagent (Invitrogen, Thermo Fisher Scientific), 5×10^3 cells were added to each well and cultured for 1 and 7 days at 37 °C, changing the media every 48 h (N=3). After each time point, the medium was removed, and 0.4 mL of a working solution (1:9 dilution of Alamar Blue in α-MEM) was added. The plate was incubated at 37 °C for 4 h in dark conditions, and, in sequence, the fluorescence (560 nm/590 nm) was recorded using a microplate reader (SpectraMax i3, Molecular Devices). PLA scaffold was the negative control, and its fluorescence on day 1 was considered 100 % of cell viability.

2.5.2. Mesenchymal stem cell proliferation

Bone marrow-derived mesenchymal stem cells (MSCs, ATCC PCS-500-012™) were cultured in a medium containing 89 % DMEM (high glucose with L-glutamine, ATCC), 10 % fetal bovine serum (FBS, ATCC) and 1 % penicillin/streptomycin (ATCC), in an incubator (Lab-Line, Barnstead) at 37°C, humidified and containing 5 % CO_2. For WST-1, LIVE/DEAD, and Phalloidin/DAPI experiments, 0.4 mL of MSCs solution was added on top of the scaffold using a 48-well plate and cultured for 1 and 7 days, changing the medium every 2-3 days.

The working solution from WST-1 assay kit (Abcam) was prepared by mixing 1 vial of lyophilized WST reagent in 5 mL of electro coupling solution (ECS). After 1 and 7 days of cell culture on the scaffolds, 20 μL of WST working solution was added to each well, and the plate was incubated at 37 °C for 4 h. The plate was shaken for 1 min, and 150 μL of each well was transferred to a 96-well plate. The absorbance was read at 440 nm using a microplate reader (FLUOstar® Omega, BMG LABTECH). PLA scaffold was the negative control, and its absorbance on day 1 was considered 100 % of cell viability.

For LIVE/DEAD assays, 50 μL of the stock solution (from LIVE/DEAD™ viability/cytotoxicity kit for mammalian cells, Thermo Fisher Scientific) was added on top of each well, and the plate was incubated at 37 °C for 30 min. After incubation, the scaffolds were turned upside down, and the images were acquired in a fluorescent microscope (Nikon TS2-LS).

For Phalloidin/DAPI assay, after 7 days, the medium was removed, 4 % paraformaldehyde (Sigma-Aldrich) was added and left for 30 min at room temperature. After 30 min, the solution was removed, and the samples were washed twice with PBS. The PBS was removed and the scaffold was added to a 0.1 % Triton X-100 (Bio-Rad) solution in PBS and kept for 15 min. In sequence, the samples were washed four times with PBS, 350 μL of Alexa Fluor 488 (Thermo Fisher Scientific) was added, and the plate was incubated for 60 min at room temperature in dark conditions. After 60 min, the samples were washed three times with PBS,

350 μL of DAPI (FluoroPure™ grade, Thermo Fisher Scientific) was added, and the plate was incubated for 15 min at room temperature in dark conditions. After 15 min, the solution was removed, and the samples were washed three times with PBS. The samples were turned upside down and analyzed using a fluorescent microscope (Nikon TS2-LS).

2.5.3. Mesenchymal stem cell differentiation

For alkaline phosphatase (ALP), alizarin red S (ARS) and PCR assays, after one day of cell seeding on the scaffolds, it was used osteogenic medium from StemPro™ Osteogenesis Differentiation Kit (Gibco™, Thermo Fisher Scientific). The osteogenic medium was prepared by mixing 100 mL of StemPro™ medium with 10 mL of StemPro™ osteogenesis supplement and 55 μL of 1 % penicillin/streptomycin (ATCC). The osteogenic medium was changed every 3-4 days.

A commercial alkaline phosphatase staining kit (Abcam) was used after 28 days of MSCs culture on the scaffolds. After cell culture, the media was removed from the wells, and the samples were washed with the kit buffer. The staining reagent was added and the plate was incubated for 30 min at 37 °C. After incubation, the samples were washed two times using the kit buffer and imaged.

The ALP activity was measured using an alkaline phosphatase assay kit (Abcam). After 14 and 28 days of MSCs culture on the scaffolds, the medium was removed, and the samples were washed with 350 μL of cold PBS. After removing the PBS, 350 μL of ALP assay buffer was added to each well, and the plate was incubated for 1 h on ice. The solutions in the wells were homogenized with pipetting, and the solutions+scaffolds were transferred to 2 mL flasks. Using a motorized tissue grinder (Fisher Scientific), the solutions+scaffolds inside the flasks were homogenized for 1 min, keeping the samples on ice. The flasks were centrifugated at 4 °C at 4400 rpm (Eppendorf centrifuge 5702 R) for 15 min. 80 μL of the supernatants were transferred to a 96-well plate, and 50 μL of 5 mM pNPP (p-nitrophenyl phosphate) solution was added to each well. The plate with samples and standards (120 μL of standards dilutions + 10 μL of ALP enzyme) was incubated for 60 min at room temperature and, after this time, 20 μL of stop solution was added to all wells. The absorbance was measured at 405 nm on a microplate reader (FLUOstar® Omega, BMG LABTECH). The amount of pNPP in the samples was obtained from the standard curve, and the ALP activity was calculated by the following equation:

$$ALP\ activity = \frac{B}{T\ V} \tag{2}$$

Where B is the amount of pNPP (μmol), T is the reaction time (60 min), and V is the sample volume (80 μL).

For ARS staining and quantification, after 14 and 28 days the medium was removed, and the cells on the scaffolds were fixed with 350 μL of 4 % formaldehyde for 30 min at room temperature. The samples were washed three times with PBS and stained with 350 μL of 2 % alizarin red S solution for 60 min at room temperature, protected from light. The alizarin red solution was prepared by mixing 1 g of alizarin red S (Sigma Aldrich) in 50 mL of distilled water and adjusting the pH to 4.1-4.3 with 2 % hydrochloric acid solution. After staining, the samples were washed three times with deionized water and imaged. For ARS quantification, 350 μL of 0.5 N HCl containing 5 % sodium dodecyl sulfate (SDS) solution was added to each well and left for 30 min. After this time, 50 μL of each sample was diluted with 150 μL of 0.5 N HCl containing 5 % SDS solution in a 96-well plate, and the absorbance was measured at 415 nm on a microplate reader (FLUOstar® Omega, BMG LABTECH).

2.5.4. RT-qPCR

Bone-related gene expression of the cells was further assessed by real-time quantitative polymerase chain reaction (RT-qPCR). After 28 days of MSCs culture on the scaffolds, the medium was removed, and 1 mL of QIAzol lysis reagent (Qiagen) was added in each well. The plate was incubated at room temperature for 20 min, and after this time, the solution with scaffold was transferred to 2 mL centrifuge tube. A motorized tissue grinder (Fisher Scientific) was applied for 30 s inside the flask immersed on ice to homogenize the solution and further extract the RNA. The solution was centrifugated at 4,400 rpm for 5 min at 4 °C (Eppendorf centrifuge 5702 R), and the supernatant was transferred to a new tube. 1 mL of 70 % ethanol was added and mixed well by pipetting. The solution was placed in a spin column from the RNeasy Kit (Qiagen) and the RNA was extracted and purified *via* the procedure provided by the kit manufacturer. The RNA concentration obtained for each sample was measured using a NanoDrop spectrophotometer (Thermo Scientific). The samples were stored at -80 °C until use. The RNA was reverse transcribed into complementary DNA (cDNA) using the SuperScript™ IV VILO Master Mix (Thermo Fisher Scientific), according to the manufacturer's instructions. Primers (Table S2) were purchased from Integrated DNA Technologies (IDT) and Sigma. RT-qPCR was performed in a QuantStudio™ 7 Flex Real-Time PCR System (Thermo Fisher Scientific) using the Applied Biosystems™ SYBR™ Green PCR Master Mix (Thermo Fisher Scientific). Glyceraldehyde 3-phosphate dehydrogenase (GAPDH) was used as the housekeeping gene. A pure PLA sample was used as control. The level of expression for each gene of interest (BMP2, OCN, OPN, COL1A1, ALPL and RUNX2) was calculated using the measured cycle threshold (Ct) values with the following equations:

$$\Delta Ct = Ct\ (\text{gene of interest}) - Ct\ (GAPDH) \tag{3}$$

$$\Delta\Delta Ct = \Delta Ct\ (\text{sample}) - \Delta Ct\ (\text{control}) \tag{4}$$

$$\text{Fold gene expression} = 2^{-\Delta\Delta Ct} \tag{5}$$

2.6. Statistical analysis

The data are reported as mean ± standard deviation and analyzed using one-way analysis of variance (ANOVA) followed by Tukey's test, in GraphPad Prism software.

3. Results

3.1. Characterization of cerium oxide nanoparticles

Prior to filament and scaffold production, the CeNPs were characterized by TEM, XPS and zeta potential measurement (Fig. 1a–c). They presented a size of 18 ± 5 nm as observed by TEM, within the range provided by the supplier (15-30 nm), and zeta potential of 24.4 mV. XPS data and analysis were applied to extract the Ce^{3+}/Ce^{4+} value, which was determined to be 13.70 % Ce^{3+}. The presence of 13.70 % of Ce^{3+} yielded an SOD-mimetic activity of 6 %.

3.2. Thermal and rheological behavior of the filaments

After characterization, the nanoparticles were mixed with the PLA and TCP and extruded in the form of filaments for additive manufacturing. Before scaffold printing, the filaments with different compositions were characterized by thermal and rheological techniques to evaluate the polymeric structure (stability, decomposition, and crystallization) and to predict the material printability. DSC and TGA results are shown in Fig. 1 and Table S3. The pure PLA and the PLA-TCP composites presented similar thermal properties, with glass transition temperature (T_g) of 60 °C, cold crystallization temperature (T_{cc}) of 127 °C, melting temperature (T_m) of 150 °C, and crystallization degree (X_c) near 1 %. The addition of CeO_2 led to a slight decrease in T_g from 60 °C for PLA-TCP to 58 °C for PLA-TCP-10CeO_2) and an increase in T_{cc} from 127 °C for PLA-TCP to 133 °C for PLA-TCP-10CeO_2), while keeping the values of T_m constant. The presence of ceramic particles in such large quantities affects the mobility of polymer chains, leading to shifted T_{cc} values. A reduction in the crystallization degree was observed with the addition of CeNPs (up to 0.29 % for 10 % CeO_2 concentration) since the

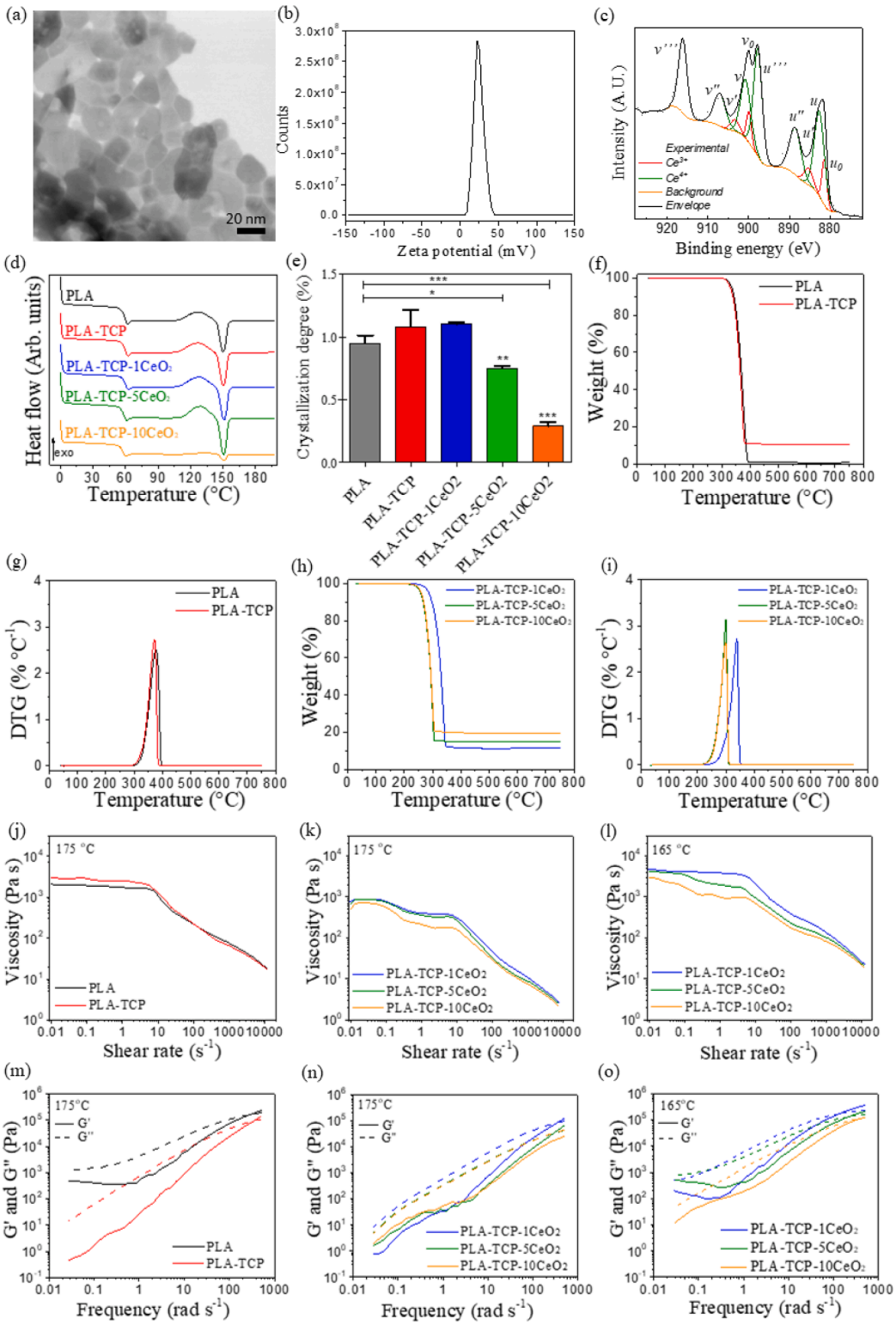

Fig. 1. (a) TEM image showing the size of the CeNPs with 18 ± 5 nm. (b) Zeta potential measurement of the CeNPs displaying value of 24.4 mV. (c) Ce 3d XPS spectra of the CeNPs presenting 13.70 % of Ce^{3+} and 86.30 % of Ce^{4+}. (d) DSC curves obtained in the second heating, (e) calculated degree of crystallinity from DSC results (compared to the PLA-TCP matrix unless identified with bars, N = 3; *: p <0.05; **: p <0.01; ***: p <0.005). (f) TGA and (g) DTG curves of the PLA and PLA-TCP samples. (h) TGA and (i) DTG curves of the samples containing CeNPs. Steady-state rheology measured from the filaments at (j-k) 175 °C and (l) 165 °C. Dynamic-state rheology measured from the filaments at (m-n) 175 °C and (o) 165 °C.

presence of additives can hinder the packing/arrangement of the polymer chains.

TGA results provide the temperature of initial decomposition (T_{onset}), the temperature of maximum decomposition (T_{max}) and residue at 750 °C. The residue corresponds to the amount of inorganic phase in the nanocomposite due to the complete decomposition of PLA at high temperatures. All samples presented residue values similar to the nominal values, showing that the amount of TCP and CeNPs added was

effectively mixed within the polymer matrix. The PLA-TCP composite presented values of T_{onset} and T_{max} close to those of pure PLA (350 °C and 376 °C, respectively), which indicates the absence of polymer degradation during processing for filament manufacturing. Samples containing CeNPs decreased T_{onset} (up to 276 °C for PLA-TCP-10CeO_2) and T_{max} (up to 298 °C for PLA-TCP-10CeO_2), probably due to polymer degradation in the presence of the additive. It is well known that metal oxides can induce thermal degradation of PLA by unzipping depolymerization [31]. A similar effect on thermal degradation was reported for cerium oxide incorporation in PLA [32]. The negative-charged oxygen from PLA chain interacts with positive-charged cerium atoms from CeNPs, while the oxygen from CeNPs interacts with the carbon from the PLA carboxyl group, leading to a catalytic depolymerization. These values of T_{onset} and T_{max} are still far higher than the printing temperature (175 °C); therefore, the presence of CeNPs do not limit the composite printability.

Rheological measurements provide important insights into filament printability. Fig. 1 and Table S4 present the results from steady and dynamic-state measurements. First, measurements were performed at 175 °C, a standard temperature for PLA printing. In the steady-state, the pure PLA presents a Newtonian plateau at low shear rates (initial viscosity value, η_0, of 2020 Pa s) and a strong linear decay at a high shear rate (power-law index n = 0.20); the addition of TCP led to an increase in viscosity (η_0, of 2960 Pa s) at low shear rates, due to physical restriction caused by these microparticles. However, no significant difference is observed between PLA and PLA-TCP curves at a high shear rate. With the incorporation of CeNPs, mainly at 5 and 10 %, a large decrease in viscosity was observed over the whole shear range, probably due to polymer degradation, as observed through the TGA result.

The shear rate on the 3D printer is dependent on the printing speed and nozzle size. However, for similar experimental setups to those of the presented study, the commonly applied shear rates are in the order of 10^2 to 10^3 s^{-1} [33]. To achieve similar viscosity of the PLA and PLA-TCP samples, the temperature of analyses and the printing process were decreased to 165 °C. At lower temperatures, the viscosity of the samples containing CeNPs increased, achieving values close to the PLA and PLA-TCP.

The storage (G') and loss (G") moduli were evaluated as a function of the oscillation frequency (ω, between 0.02 and 500 rad s^{-1}). The elastic behavior (G'>G'') of the materials favors high accuracy in the scaffold printing geometry, relative to design specifications. For good printability, polymeric materials should present high G' values; being, in the least close to G", but preferably higher than G". All samples, at both 175 °C and 165 °C, presented predominantly viscous behavior (G''>G') at low oscillation frequencies. The increase in frequency implies a shorter response time of the material to the applied deformation. Therefore, an inversion of behavior (G'>G") was observed at high frequencies (Table S4), except for the PLA-TCP-10CeO_2 at 175 °C, confirming the need to lower the temperature for 3D printing filaments containing CeNPs to achieve a high level of printing fidelity. The decrease of the temperature to 165 °C led to the appearance of the inversion point (G'>G") for the PLA-TCP-10CeO_2 sample.

3.3. Scaffolds for bone tissue engineering

As previously described, the thermal and rheological properties of the material play an important role during the printing process and by adapting the temperature, it was possible to optimize the printability of the scaffolds containing CeO_2. The scaffolds of pure PLA and PLA-TCP were printed at 175 °C, while the scaffolds containing 1, 5 and 10 % CeO_2 were printed at 165 °C. All scaffolds presented accurate shape and size compared to the designed geometry with a pore size of 300 μm, strut height of 300 μm and strut width of 400 μm (Figs. 2a–c and S1). EDS mapping (Figs. 2b and S2) shows that the TCP and CeNPs are homogeneously dispersed within the polymeric matrix. The fabrication of filaments *via* extrusion and the re-melting occuring in the additive manufacturing process favors the homogenization of the nanocomposites, which is of utmost importance to achieve reproducible outcomes.

The presence of ceria in the scaffold was also confirmed by XRD spectra (Fig. 2d). The PLA-TCP-10CeO_2 sample presented signals at 28, 33, 47 and 56 degrees (2θ): ascribable to the CeO_2 fluorite-type crystal structure. Signal peaks at 27, 31 and 34 degrees are further ascribed to TCP and the broad band between 10 and 25 degrees is related to the presence of PLA. XPS results also confirmed the presence of PLA, TCP and CeO_2 in the PLA-TCP-10CeO_2 scaffold. The XPS Ce 3d spectra (Fig. 2e) was used to obtain the Ce^{3+}/Ce^{4+} ratio in the nanocomposite, determined to be 30.39 % Ce^{3+}.

Compression testing was performed to obtain the elastic modulus of the scaffolds (Fig. 2f). The pure PLA scaffold presented an elastic modulus of 73 MPa. Incorporation of TCP led to a value of 83 MPa, which is not statistically different from PLA considering $p<0.05$. The addition of 1 and 5 % of CeO_2 did not cause a significant change in the PLA-TCP elastic modulus; however, the addition of 10 % CeO_2 led to an increase of 27 % ($p<0.005$), achieving a value of 105 MPa. Compared to the pure PLA scaffold, the PLA-TCP-10CeO_2 presented an increase of 44 % ($p<0.005$). Although the incorporation of CeNPs led to polymeric degradation, as observed by TGA and rheometry, the extent was not substantial enough to influence the mechanical properties. On the contrary, the high elastic modulus of cerium oxide benefited the mechanical resistance of the composite. This improvement is another confirmation of the homogenous dispersion of the additives in the polymeric matrix, since agglomerated particles may act as stress concentration centers, resulting in decreased mechanical properties [34].

A similar result was obtained from protein adsorption assay (Fig. 2g), with no significant difference between PLA-TCP and pure PLA, PLA-TCP-1CeO_2 and PLA-TCP-5CeO_2. However, the PLA-TCP-10CeO_2 samples presented 46 % increase in protein adsorption compared to PLA-TCP ($p<0.05$) and 49 % increase compared to pure PLA scaffold ($p<0.05$).

The degradation of the composites was analyzed in PBS, PBS containing proteinase and culture medium, as a function of time (Fig. 2h-j). In PBS, up to 275 days, almost no weight loss was observed for all samples, however in the presence of proteinase, it was possible to observe an accelerated degradation for the samples containing CeNPs, as expected. The weight loss scales with the amount of CeNPs, with higher amounts of CeNPs yielding faster degradation ratio kinetics. In culture medium the samples did not degrade up to 28 days, which is the maximum period used for the cell assays. ICP-MS measurements of cerium content, leeched into osteogenic culture media after 14 and 28 days, corroborate these measurements: showing < 0.5 wt % (relative to cerium content in as-fabricated scaffolds) total release by 28 days for all scaffold compositions (data not shown).

3.4. Evaluation of the cytocompatibility and osteogenic behavior of the scaffolds

Osteoblast cell adhesion was evaluated after 1 day of cell culture on the scaffolds using scanning electron microscopy. Representative SEM images display the positive effect of CeNPs on cell adhesion. PLA-TCP-1CeO_2, PLA-TCP-5CeO_2, and PLA-TCP-10CeO_2 samples reveal greater cell spreading and with extended growth of filopodia, compared to PLA and PLA-TCP (Fig. 3a). Cell viability was assessed after 1 and 7 days of osteoblast and MSCs culture on the scaffolds (Fig. 3b-c). The presence of nanoceria enhanced cell viability after 7 days for both types of cells compared to PLA and PLA-TCP. The presence of 10 % CeNPs led to a 36 % increase in osteoblast viability compared to PLA ($p<0.01$) and 23 % increase compared to PLA-TCP ($p<0.05$), after 7 days. For MSCs after 7 days, the PLA-TCP-10Ce scaffold led to an increase in cell viability of 6 % ($p<0.05$) and 7 % ($p<0.01$) compared to PLA and PLA-TCP, respectively. The positive effect of CeNPs on cell proliferation was assessed by cell counting using DAPI nuclei staining (Fig. S3). The significant proliferation of MSCs, especially for the samples containing CeNPs, was

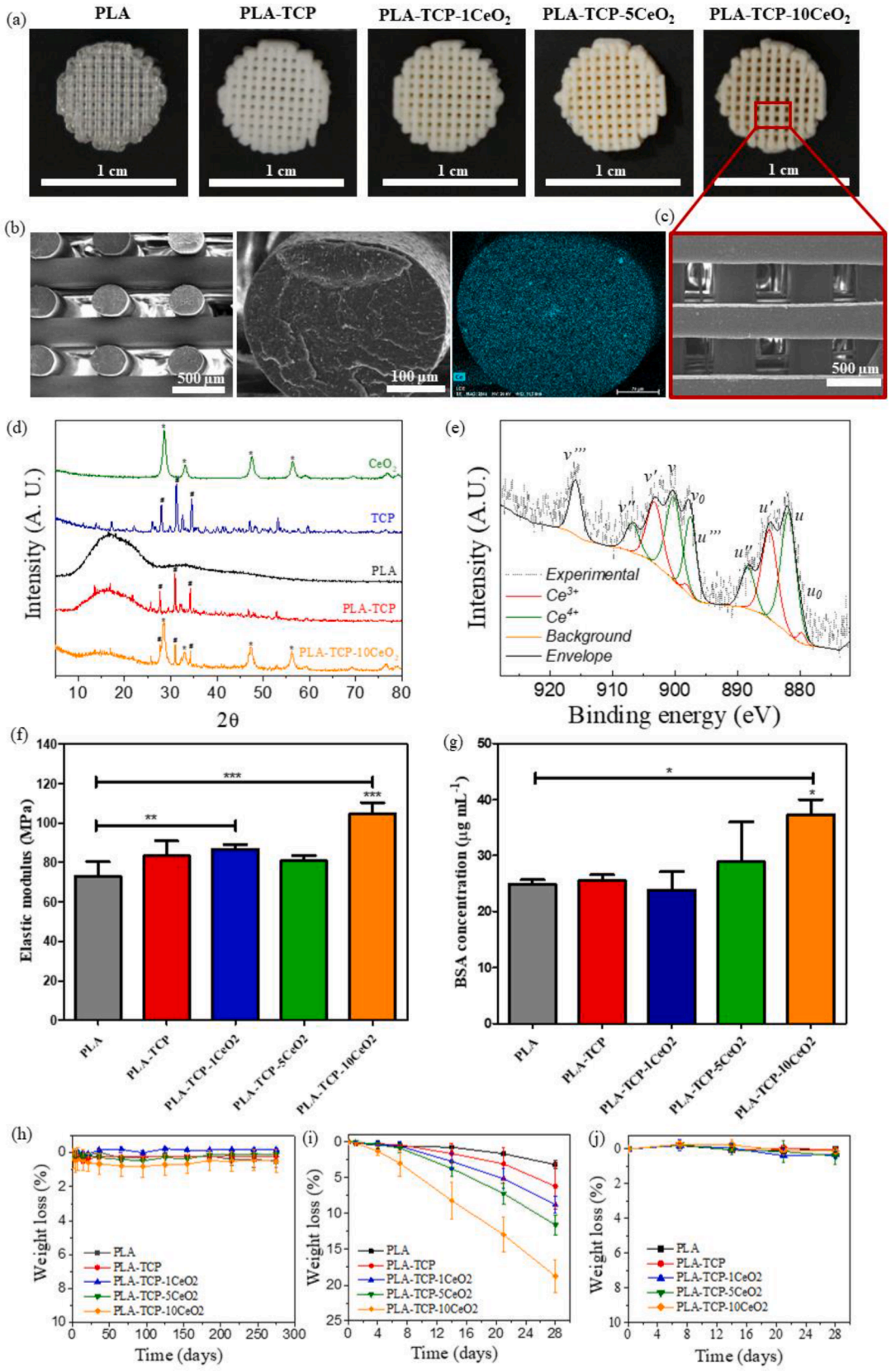

Fig. 2. (a) Photo of the scaffolds. (b) Cross-sectional SEM-EDS and (c) top view SEM of the PLA-TCP-10CeO_2 scaffold. (d) XRD of the CeNPs powder, TCP powder and the PLA, PLA-TCP and PLA-TCP-10CeO_2 scaffolds. (e) Ce 3d XPS spectra of the PLA-TCP-10CeO_2 scaffold showing the presence of 30.39 % of Ce^{3+}. (f) Elastic modulus extracted from the linear region of the stress-strain curves in compression mode (N = 5). (g) Protein adsorption to scaffold samples (N=3). Degradation in (h) PBS, (i) PBS containing proteinase and (j) culture medium, as a function of time (N=3). The data are expressed as mean ± standard deviation and compared to the PLA-TCP matrix unless identified with bars. (*: $p < 0.05$; **: $p < 0.01$; ***: $p < 0.005$).

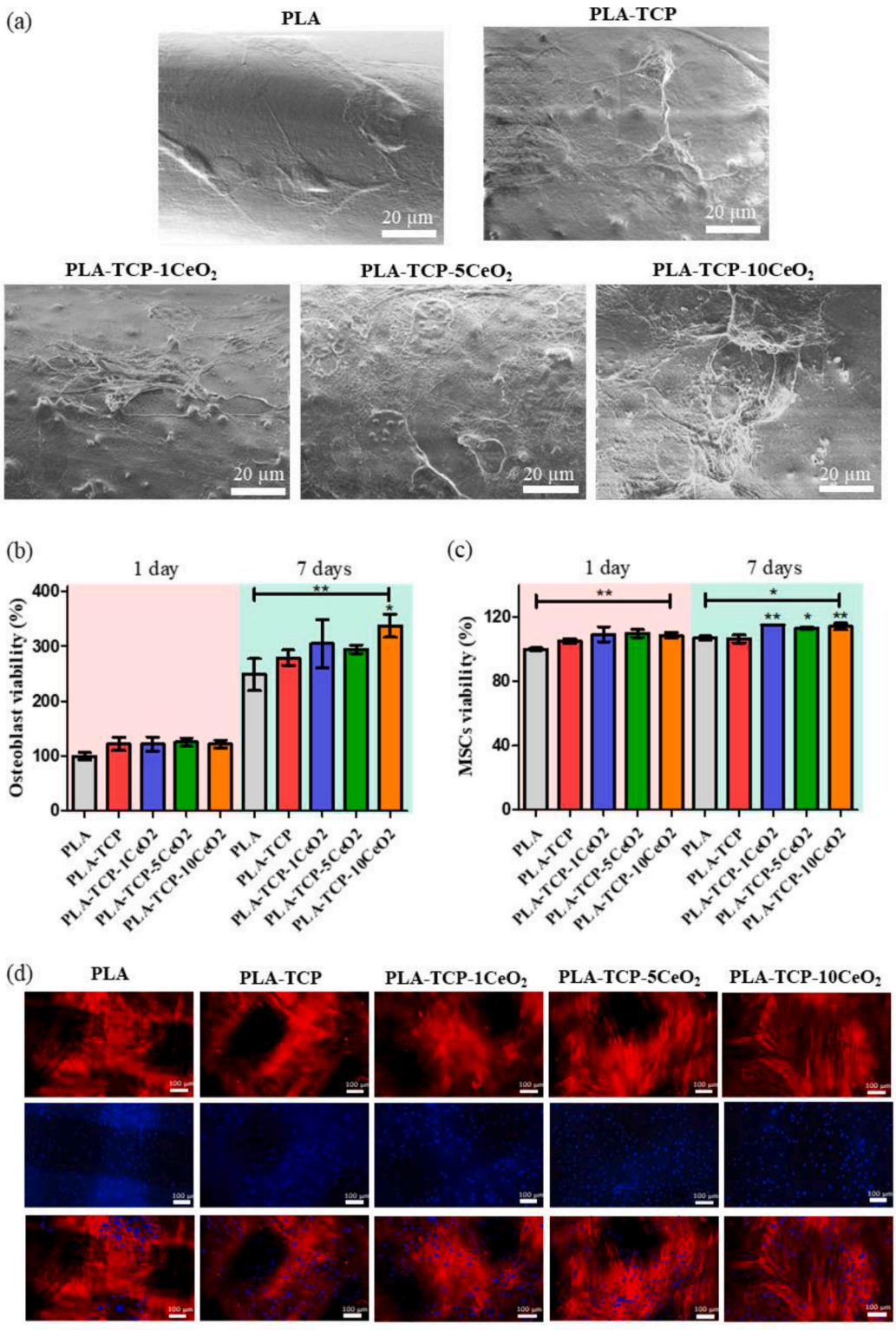

Fig. 3. (a) SEM images of the osteoblasts adhered to the scaffold surface after 1 day of cell culture. Cytotoxicity evaluation after 1 and 7 days of (b) osteoblast culture and (c) MSCs culture on the scaffolds. The data are expressed as mean ± standard deviation and compared to the PLA-TCP matrix at the same time point unless identified with bars. (N = 3; *: $p < 0.05$; **: $p < 0.01$; ***: $p < 0.005$). (d) Representative fluorescence micrographs after 7 days of MSCs culture on the scaffolds, showing substantial cell proliferation for all samples. Alexa Fluor 488 Phalloidin was used to stain the cytoskeleton of cells in red, and DAPI nuclei staining appear in blue.

visualized by fluorescence microscopy after staining with Phalloidin/DAPI (Fig. 3d). LIVE/DEAD assay (Fig. S4), performed after 1 and 7 days of MSCs culture on the scaffolds, also confirmed the scaffold non-cytotoxicity with the absence of dead cells (red) and the presence of live cells (green).

Alizarin Red S (ARS) staining and quantification assay were employed for assessing calcium deposition during mesenchymal stem cell differentiation into osteoblasts. ARS is a specific dye that binds to

calcium ions within the mineralized extracellular matrix produced by osteoblasts, allowing for the visualization of calcified nodules. After staining, the nodules appear as distinctive red deposits, providing a qualitative assessment of osteogenic differentiation. To quantitatively analyze calcium deposition, ARS-stained nodules were solubilized, and the dye was extracted and quantified spectrophotometrically. The absorbance values directly correlate with the amount of calcium present, enabling a precise and reproducible measurement of osteogenic differentiation. Qualitative analysis by ARS staining revealed a more intense calcium deposition on the scaffolds containing CeNPs after 28 days of MSCs culture (Fig. 4a). The quantitative analysis confirmed this result (Fig. 4c), with increasing mineralization for 1, 5 and 10 % CeO_2-containing samples, compared to the PLA-TCP matrix. The PLA-TCP-10CeO_2 composition after 28 days of cell culture presented an almost 3-fold increase in mineralization compared with the PLA-TCP matrix. Interestingly, the PLA-TCP matrix showed a significant enhancement of the mineral content compared to pure PLA for 14 and 28 days, as expected, due to the presence of osteogenic calcium phosphate. The levels of ALP activity also intensified in the presence of CeNPs after 28 days of MSCs culture compared with the PLA-TCP scaffold (Fig. 4b and 4d). The presence of 1, 5 and 10 wt % of CeNPs led to an increase in ALP activity of 20 % (**: $p < 0.01$), 31 % ($p < 0.005$) and 21 % (**: $p < 0.01$) compared to the PLA-TCP matrix, respectively. RT-qPCR results (Fig. 4e-j) confirmed the osteogenic behavior of CeNPs, showing for PLA-TCP-10CeO_2 up-regulated BMP2, ALPL, OCN and OPN expression, compared to PLA-TCP.

4. Discussion

The size, morphology and surface charge of CeNPs play fundamental roles in defining particle physico-chemical properties [22,35]. Patil and co-workers [35] have detailed the effect of CeNPs zeta potential on the adsorption of bovine serum albumin (BSA). Positive zeta potential was found to adsorb more of the protein, while CeNPs with negative zeta potential showed little or no protein adsorption [35]. Therefore, the positive value measured for the CeNPs of 24.4 mV is beneficial for protein adsorption and consequently, cell adhesion. This assumption was confirmed by our own protein adsorption assay. After 24 h in contact with BSA, the scaffold containing 10 % of CeNPs adsorbed 46 % more proteins than the PLA-TCP matrix. The large surface area:volume ratio of CeNPs tends to induce substantial protein adsorption [35], yielding this increase. In addition, as cited above, CeNPs with positive zeta potential, such as those dispersed in biological media at physiological pH (*i.e.*, less than the material's isoelectric point or point of zero charge; generally, pH<8 for small spherical particles), tend to absorb negatively-charged proteins, such as serum albumin, which is the most abundant protein found in human blood [35]. When a foreign material is implanted in the body, proteins first adsorb on the material and then, in sequence, cells bind with the adsorbed proteins and adhere to the surface. Therefore, the enhanced protein adsorption observed for ceria-containing sample is an indicative of better cell proliferation.

The wettability of the scaffolds might also influence protein adsorption, and consequently, cell proliferation [3], however no statistically significant difference was observed between pure PLA, the PLA-TCP matrix and the scaffolds containing CeNPs (Fig. S5). All samples presented contact angle values close to 90°.

Another important metric concerning the CeNPs character is the Ce^{3+}/Ce^{4+} states ratio, which influences the antioxidant property of the material. The CeNPs regenerative properties come from the coexistence of Ce^{3+}/Ce^{4+} states and their low reduction potential that facilitates the conversion between them [22]. In a recent review, Das and coauthors have described the antioxidant property of CeNPs in biological systems [22]. CeNPs with high Ce^{3+}/Ce^{4+} ratios favor the superoxide dismutase (SOD) mimetic activity, which is responsible for scavenging superoxide ($^{\bullet}O_2^-$) and hydroxyl ($^{\bullet}OH$) radicals, whereas low Ce^{3+}/Ce^{4+} promotes the scavenging of hydrogen peroxide (H_2O_2) and nitric oxide radical ($^{\bullet}NO$) by catalase mimetic activity [22]. Both mechanisms favor the scavenging of reactive oxygen species (ROS), assisting the regenerative process in the biological system. The antioxidant activity of CeNPs is effective against inflammation, protecting cells or tissue from damage. In addition, free radical formation during cellular proliferation hinders cell differentiation; therefore, the presence of CeNPs can enhance cell growth by acting as antioxidants [22]. The CeNPs presented 13.70 % of Ce^{3+}, however, when incorporated in the PLA-TCP-10CeO_2, this value increased to 30.39 %.

The presence of mixed cerium valence surface sites has been shown in other studies to promote therapeutic efficacy in osteogenic applications. Specifically, one study found redox state ratio to affect cell spreading, migration, and adhesion to a PLA-coated surface by an osteoblast (MG63) and a mesenchymal stem cell line [36]. Interestingly, the Ce^{3+}/Ce^{4+} value for the composite is 121.84 % (factor of 2.22) of the value for the powder CeNP control. In comparing the Ce 3d spectrum of the complete composite with that of the pure powder, there is a significant increase in relative intensity at the Ce^{3+}-associated *u'* feature. This higher binding energy peak, within the $Ce3d_{5/2}$ envelope, has been ascribed to an excited state configuration stabilized by charge-transfer from a coordinating ligand (nearest neighbor site), such as oxygen in ceria [37,38].

To identify the cause of this increase in the fraction of cerium sites in a reduced state, control XPS measurements were performed for powder CeNPs and for a powder mixture of CeNPs with TCP heated to 200 °C, *in situ*, under vacuum (Fig. S6). Neither spectrum demonstrated significant increase in measured Ce^{3+} population, relative to as-obtained CeNP powder. Results from these studies suggest the observed material behavior is not a direct consequence of CeNP heating, during filament formation or printing, or of CeNP chemical interaction with TCP. However, effects from physical environment and the known affinity of phosphates towards ceria cannot be completely discounted in considering particle surface chemistry in the PLA melt based on these observations [39,40]. Further, the presence of esther groups in the main PLA chain and carboxylic groups at the end of the PLA chain may be related to this change in chemical state, implicating cerium-PLA interactions [41].

The incorporation of CeNPs into the PLA-TCP matrix has also imparted significant effects on the thermal and rheological behavior of the composite. The decrease in the crystallization degree with the increasing amount of CeNPs favored the 3D printing process as it reduces material shrinkage during cooling, resulting in better printing accuracy. In addition, the lower crystallization degree of the composites containing high CeNPs loads is favorable for application in bone tissue engineering since the degradation kinetics are increased for amorphous PLA [42]. Another characteristic that might accelerated the degradation kinetics of the PLA-TCP-CeO_2 composites was the thermal degradation of the PLA in the presence of CeNPs after the extrusion of the filaments at high temperature. TGA results showed decreasing T_{onset} and T_{max} with increasing amounts of CeNPs.

Ideally, the material's degradation ratio applied for bone tissue regeneration should match the kinetics of bone growth. PLA has been intensely explored for medical applications; however, for bone tissue engineering, its slow degradation rate and consequent long reabsorption time may limit its application [43,44]. Copolymerization, blending, additives incorporation and irradiation have been pursued as alternatives to accelerate the PLA' ratio of degradation [44]. The PLA degradation may take months or even years, depending on the polymer molecular weight, crystallinity, and amount of D or L isomer. In addition, the scaffold pore size, interconnectivity, and geometry may also influence the composite ratio of degradation [44]. The presence of CeNPs decreased the crystallization degree and slightly degraded the polymeric structure, which imparted faster degradation. Therefore, the PLA-TCP-10CeO_2 would present the fastest reabsorption time *in vivo*, which is beneficial for bone regeneration.

The degradation of the PLA structure by CeNPs also affected the

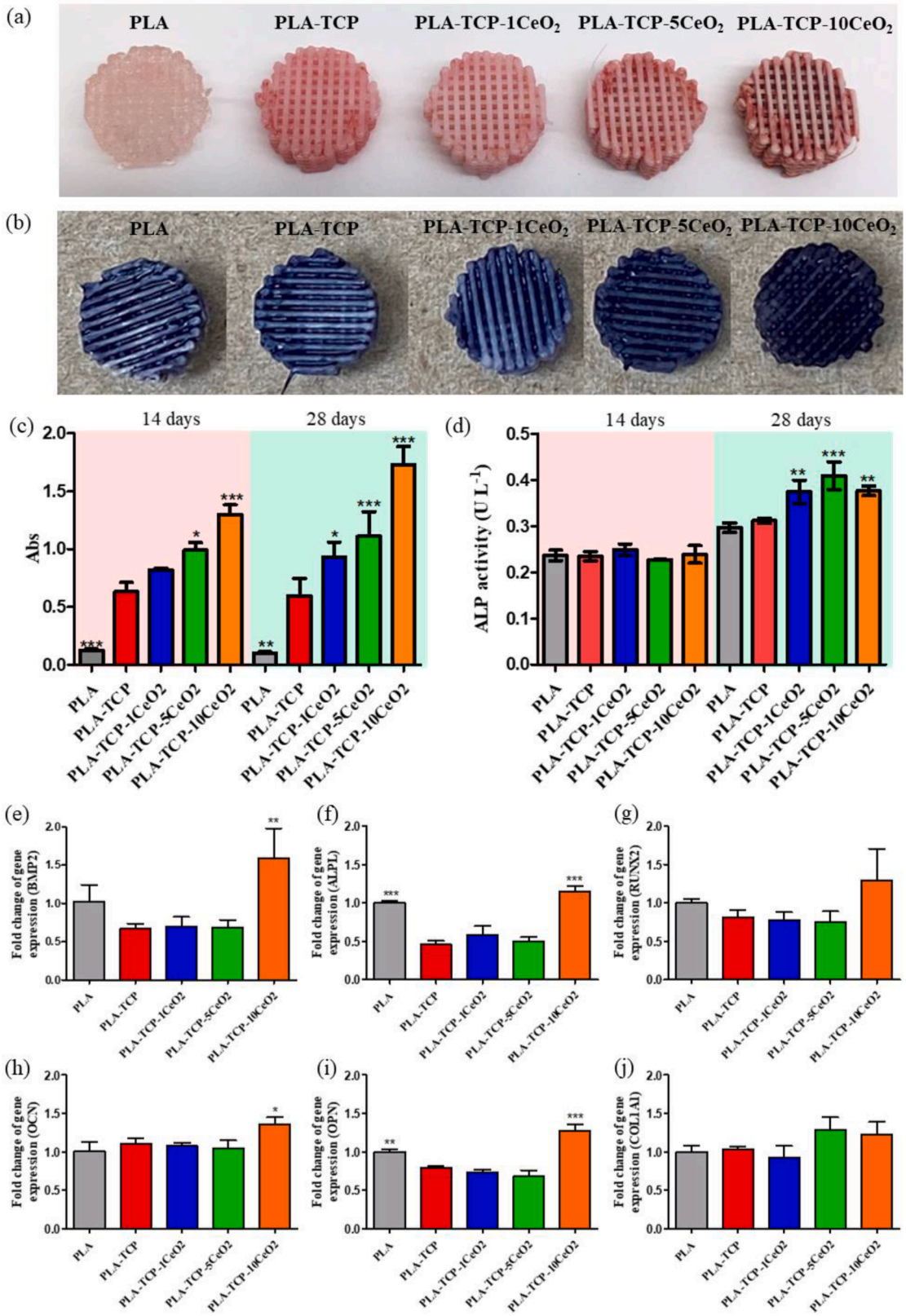

Fig. 4. Mesenchymal stem cell differentiation using an osteogenic medium. (a) Alizarin red S (ARS) staining and (b) alkaline phosphatase (ALP) staining after 28 days of MSCs culture on the scaffolds. (c) ARS quantification and (d) ALP activity after 14 and 28 days. RT-qPCR results after 28 days of MSCs culture on the scaffolds. Expression level of (e) BMP2, (f) ALPL, (g) RUNX2, (h) OCN, (i) OPN and (j) COL1A1. The data are expressed as mean ± standard deviation and compared to the PLA-TCP matrix at the same time point. (N = 3; *: $p < 0.05$; **: $p < 0.01$; ***: $p < 0.005$).

printability of the material. Typically, PLA is printed at 175 °C, but the presence of CeNPs led to decreased viscosity values. Rheological measurements were performed to optimize the material's printability. It was observed that decreasing the temperature to 165 °C, the PLA-TCP-10CeO_2 composite demonstrated a viscosity value close to the PLA-TCP at 175 °C. Therefore, by tuning the temperature of the 3D printing process, it was possible to obtain a porous 3D structure with precise geometry. The pore size of 300 μm is within the desired range for bone cell proliferation; specifically, between 150 and 500 μm [45–47]. Another essential feature for bone engineering scaffolds is the achievement of mechanical properties similar to native tissue. The porous scaffolds developed in this work presented elastic moduli between 73 and 105 MPa, similar to trabecular bone (elastic modulus of 50–500 MPa) [48].

The PLA-TCP-CeO_2 composites, specially containing 10 % of CeNPs, stimulated both osteoblast and MSCs proliferation. Furthermore, the presence of CeNPs promoted the mineralization of the extracellular matrix and enhanced the ALP activity after 14 and 28 days of MSCs culture on the scaffolds, indicating increased levels of osteogenesis. Similar results for osteogenic differentiation using CeNPs were recently reported by Nilawar and Chatterjee [49]. The authors modified 3D-printed PLA scaffolds with CeNPs using NaOH treatment, followed by covalent functionalization with poly(ethylene imine) (PEI) and citric acid through the use of carbodiimide (EDC−NHS) chemistry. In this study, we could achieve similar outcomes with an easier methodology and without additional steps after printing. In addition, the incorporation of CeNPs into the PLA structure provided advantages for mechanical behavior and degradation kinetics, as discussed above.

An in-depth investigation of stem cell differentiation was conducted by monitoring the expression alteration of osteogenic-related genes, including bone morphogenetic protein 2 (BMP2), runt-related gene 2 (RUNX2), alkaline phosphatase (ALPL), osteocalcin (OCN), osteopontin (OPN) and type I collagen (COL1A1). The presence of CeNPs led to the up-regulation of BMP2, ALPL, OCN and OPN expression, compared to PLA-TCP. Other authors have demonstrated the osteogenesis mechanism of cerium via the Smad-dependent BMP signaling pathway [50–52]. The up-regulated gene expression promotes osteogenesis of MSCs and consequently can accelerate bone healing. While CeNP-containing scaffold composites were observed to promote osteoblast and MSC proliferation, ICP-MS studies found only limited release (< 0.5 wt % cerium for all composite compositions) of CeNPs upon storing in osteogenic media for up to 28 days. Results of the study suggest that therapeutic value from the CeNP scaffold components is derived, largely, from scaffold-incorporated particles rather than released particles. Therefore, scaffolds of these or similar compositions would benefit from prolonged, local therapeutic action from incorporated CeNPs during the bone growth process. Further, this data suggests that incorporation of CeNPs at up to, at least, 10 % will not substantially affect scaffold mechanical integrity or introduce additional potential modes of failure. The data also confirm that scaffold dissolution will be slow enough to preclude toxic effects from the CeNP components.

Others researchers have explored diverse compositions of 3D scaffolds for bone repair [53–57]. Among them, composite scaffolds offer great potential by combining mechanical robustness with bioactive properties; however, achieving an ideal balance and homogenization between these components can require intricate processes, posing challenges during fabrication. Most of the works have reported the achievement of 3D printed composites scaffold using complex and toxic solvent-based methodologies [54]. Furthermore, composite scaffolds utilized in bone tissue engineering frequently combine a polymeric matrix with a single ceramic filler, predominantly calcium phosphates [55–57]. Overall, the PLA-TCP-CeO_2 composite developed here stand out for its cost-effectiveness and straightforward fabrication. PLA, TCP and CeNPs have been mixed directly during filament fabrication, without the need for organic solvents or extra procedures post-3D printing. Additionally, an effectively enhanced cell function resulted from a dual incorporation of bioactive fillers (TCP and CeNPs).

5. Conclusions

Porous 3D-printed composites were evaluated as a biomaterial for bone repair. Osteogenic nanocomposites were fabricated by integrating cerium oxide nanoparticles and tricalcium phosphate into poly (lactic acid). The use of extrusion for filament production, followed by additive manufacturing for scaffold fabrication, yielded 3D constructs with homogeneous composition. The presence of CeNPs influenced the viscosity and the viscoelastic behavior of the filaments and, using rheological characterization, it was possible to optimize the printing temperature to obtain porous scaffolds with precise geometry. The presence of 10 wt % CeNPs led to stronger mechanical properties (increase of 27 %), enhanced protein adsorption (increase of 46 %), faster degradation, and extended cell proliferation (increase of 23 %). The incorporation of CeNPs also favored the osteogenic differentiation of mesenchymal stem cells. After 28 days of cell culture, the PLA-TCP-10CeO_2 composition presented an almost 3-fold increase in calcium deposition, a 21 % increase in ALP activity, and notably up-regulated BMP2, ALPL, OCN and OPN expression *in vitro*, compared to PLA-TCP matrix. Further animal studies are needed to pursue the potential of this composite for accelerating bone regeneration. Overall, bioactive PLA-TCP-CeO_2 composite is promising as a 3D-printed scaffold for bone repair. The possibility to store the filaments with ready-to-use composition favors its application in future healthcare centers or remote locations. In addition, the easy, affordable, and customized production of bone implants by additive manufacturing may overcome the drawbacks of traditional therapies.

CRediT authorship contribution statement

Samarah V. Harb: Conceptualization, Data curation, Investigation, Methodology, Writing – original draft, Writing – review & editing. **Elayaraja Kolanthai:** Investigation, Methodology, Supervision, Writing – review & editing. **Abinaya S. Pugazhendhi:** Formal analysis, Investigation. **Cesar A.G. Beatrice:** Formal analysis, Investigation, Writing – original draft. **Leonardo A. Pinto:** Data curation, Methodology, Validation. **Craig J. Neal:** Data curation, Formal analysis, Investigation, Writing – review & editing. **Eduardo H. Backes:** Conceptualization, Methodology, Visualization. **Ana C.C. Nunes:** Data curation, Investigation. **Heloisa S. Selistre-de-Araújo:** Conceptualization, Funding acquisition, Resources. **Lidiane C. Costa:** Conceptualization, Formal analysis, Methodology, Writing – review & editing. **Melanie J. Coathup:** Conceptualization, Resources, Visualization. **Sudipta Seal:** Funding acquisition, Resources, Supervision, Writing – review & editing. **Luiz A. Pessan:** Conceptualization, Funding acquisition, Resources, Supervision, Writing – review & editing.

Declaration of Competing Interest

The authors declare that they have no known competing financial interests or personal relationships that could have appeared to influence the work reported in this paper.

Data availability

Data will be made available on request.

Acknowledgments

This work was supported by Coordenação de Aperfeiçoamento de Pessoal de Nível Superior (CAPES) - Finance Code 001, Conselho Nacional de Desenvolvimento Científico e Tecnológico (CNPq) and Fundação de Amparo à Pesquisa do Estado de São Paulo (FAPESP) (grant numbers 2018/26060-3, 2017/11366-7, 2017/09609-9, 2019/27415-

2, 2021/11538-8). The authors thank the Laboratory of Structural Characterization (LCE/DEMa/UFSCar) for access to SEM-EDS facilities. NSF MRI Grant: ECCS (grant no. 1726636) funding for XPS measurements. E.K., A.S.P, and C.J.N. acknowledge the UCF Preeminent Postdoctoral Program (P3) for funding support.

Supplementary materials

Supplementary material associated with this article can be found, in the online version, at doi:10.1016/j.bbiosy.2023.100086.

References

[1] Koons GL, Diba M, Mikos AG. Materials design for bone-tissue engineering. Nat Rev Mater 2020;5:584–603.
[2] Collignon AM, Lesieur J, Vacher C, Chaussain C, Rochefort GY. Strategies developed to induce, direct, and potentiate bone healing. Front Physiol 2017;8:927.
[3] Harb SV, Uvida MC, Trentin A, Lobo AO, Webster TJ, Pulcinelli SH, Santilli CV, Hammer P. PMMA-silica nanocomposite coating: effective corrosion protection and biocompatibility for a Ti6Al4V alloy. Mater Sci Eng C 2020;110:110713.
[4] Wang W, Yeung KWK. Bone grafts and biomaterials substitutes for bone defect repair: a review. Bioact Mater 2017;2:224–47.
[5] Wang C, Huang W, Zhou Y, He L, He Z, Chen Z, He X, Tian S, Liao J, Lu B, Wei Y, Wang M. 3D printing of bone tissue engineering scaffolds. Bioact Mater 2020;5:82–91.
[6] E..H Harb BSV, Beatrice CAG, Shimomura KMB, Passador FR, Costa LC, Pessan LA. Polycaprolactone usage in additive manufacturing strategies for tissue engineering applications: a review. J Biomed Mater Res B Appl Biomater 2022;110:1479–503.
[7] Mumith A, Thomas M, Shah Z, Coathup M, Blunn G. Additive manufacturing: current concepts, future trends. Bone Joint J 2018;100:455–60.
[8] Mirkhalaf M, Men Y, Wang R, No Y, Zreiqat H. Personalized 3D printed bone scaffolds: a review. Acta Biomater 2023;156:110–24.
[9] Chou YC, Lee D, Chang TM, Hsu YH, Yu YH, Liu SJ, Ueng SW. Development of a three-dimensional (3D) printed biodegradable cage to convert morselized corticocancellous bone chips into a structured cortical bone graft. Int J Mol Sci 2016;17:595–608.
[10] Dussault A, Pitaru AA, Weber MH, Haglund L, Rosenzweig DH, Villemure I. Optimizing design parameters of PLA 3D-printed scaffolds for bone defect repair. Surgeries 2022;3:162–74.
[11] Donate R, Monzón M, Alemán-Domínguez ME. Additive manufacturing of PLA-based scaffolds intended for bone regeneration and strategies to improve their biological properties. e-Polymers 2020;20:571–99.
[12] Backes EH, Pires LN, Selistre-de-Araujo HS, Costa LC, Passador FR, Pessan LA. Development and characterization of printable PLA/β-TCP bioactive composites for bone tissue applications. J Appl Polym Sci 2020;138:e49759.
[13] Bernardo MP, da Silva BCR, Hamouda AEI, de Toledo MAS, Schalla C, Rütten S, Goetzke R, Mattoso LHC, Zenke M, Sechi A. PLA/hydroxyapatite scaffolds exhibit *in vitro* immunological inertness and promote robust osteogenic differentiation of human mesenchymal stem cells without osteogenic stimuli. Sci Rep 2022;12:2333.
[14] Backes EH, Fernandes EM, Diogo GS, Marques CF, Silva TH, Costa LC, Passador FR, Reis RL, Pessan LA. Engineering 3D printed bioactive composite scaffolds based on the combination of aliphatic polyester and calcium phosphates for bone tissue regeneration. Mater Sci Eng C 2021;122:111928.
[15] Wang W, Zhang B, Li M, Li J, Zhang C, Han Y, Wang L, Wang K, Zhou C, Liu L, Fan Y, Zhang X. 3D printing of PLA/n-HA composite scaffolds with customized mechanical properties and biological functions for bone tissue engineering. Compos B Eng 2021;224:109192.
[16] Liu Z, Ge Y, Zhang L, Wang Y, Guo C, Feng K, Yang S, Zhai Z, Chi Y, Zhao J, Liu F. The effect of induced membranes combined with enhanced bone marrow and 3D PLA-HA on repairing long bone defects *in vivo*. J Tissue Eng Regen Med 2020;14:1403–14.
[17] Zhang B, Wang L, Song P, Pei X, Sun H, Wu L, Zhou C, Wang K, Fan Y, Zhang X. 3D printed bone tissue regenerative PLA/HA scaffolds with comprehensive performance optimizations. Mater Des 2021;201:109490.
[18] Lu B, Zhu DY, Yin JH, Xu H, Zhang CQ, Ke QF, Gao Y, Guo YP. Incorporation of cerium oxide in hollow mesoporous bioglass scaffolds for enhanced bone regeneration by activating ERK signaling pathway. Biofabrication 2019;11:025012.
[19] Li K, Shen Q, Xie Y, You M, Huang L, Zheng X. Incorporation of cerium oxide into hydroxyapatite coating regulates osteogenic activity of mesenchymal stem cell and macrophage polarization. J Biomater Appl 2017;31:1062–76.
[20] Xiang J, Li J, He J, Tang X, Dou C, Cao Z, Yu B, Zhao C, Kang F, Yang L, Dong S, Yang X. Cerium oxide nanoparticle modified scaffold interface enhances vascularization of bone grafts by activating calcium channel of mesenchymal stem cells. ACS Appl Mater Interfaces 2016;8:4489–99.
[21] Singh S, Kumar U, Gittess D, Sakthivel TS, Babu B, Seal S. Cerium oxide nanomaterial with dual antioxidative scavenging potential: synthesis and characterization. J Biomater Appl 2021;36:834–42.
[22] Das S, Dowding JM, Klump KE, McGinnis JF, Self W, Seal S. Cerium oxide nanoparticles: applications and prospects in nanomedicine. Nanomedicine 2013;8:1483–508.
[23] Manlin Q, Wen L, Xufeng Z, Xue L, Yue S, Yu W, Chunyan L, Lin W. Cerium and its oxidant-based nanomaterials for antibacterial applications: a state-of-the-art review. Front Mater 2020;7:213.
[24] Alpaslan E, Geilich BM, Yazici H, Webster TJ. pH-controlled cerium oxide nanoparticle inhibition of both gram-positive and gram-negative bacteria growth. Sci Rep 2017;7:45859.
[25] Putri GE, Rilda Y, Syukri S, Labanni A, Arief S. Highly antimicrobial activity of cerium oxide nanoparticles synthesized using Moringa oleifera leaf extract by a rapid green precipitation method. J Mater Res Technol 2021;15:2355–64.
[26] Zambon A, Malavasi G, Pallini A, Fraulini F, Lusvardi G. Cerium containing bioactive glasses: a review. ACS Biomater Sci Eng 2021;7:4388–401.
[27] Nicolini V, Gambuzzi E, Malavasi G, Menabue L, Menziani MC, Lusvardi G, Pedone A, Benedetti F, Luches P, D'Addato S, Valeri S. Evidence of catalase mimetic activity in Ce^{3+}/Ce^{4+} doped bioactive glasses. J Phys Chem B 2015;119:4009.
[28] Kurtuldu F, Mutlu N, Michálek M, Zheng K, Masar M, Liverani L, Chen S, Galusek D, Boccaccini AR. Cerium and gallium containing mesoporous bioactive glass nanoparticles for bone regeneration: bioactivity, biocompatibility and antibacterial activity. Mater Sci Eng C 2021;124:112050.
[29] Mandoli C, Pagliari F, Pagliari S, Forte G, Di Nardo P, Licoccia S, Traversa E. Stem cell aligned growth induced by CeO_2 nanoparticles in PLGA scaffolds with improved bioactivity for regenerative medicine. Adv Funct Mater 2010;20:1617.
[30] Santos LG, Costa LC, Pessan LA. Development of biodegradable PLA/PBT nanoblends. J Appl Polym Sci 2017;135:45951.
[31] Fan Y, Nishida H, Mori T, Shirai Y, Endo T. Thermal degradation of poly(L-lactide): effect of alkali earth metal oxides for selective L,L-lactide formation. Polymer 2004;45:1197–205.
[32] Wu Y, Hao X, Lin F, Wang S, Chen L, Lin X, Gan D, Fan S, Song L, Liu Y. Developing a cerium lactate antibacterial nucleating agent for multifunctional polylactic acid packaging film. Int J Biol Macromol 2022;220:56–66.
[33] Sanchez LC, Beatrice CAG, Lotti C, Marini J, Bettini SHP, Costa LC. Rheological approach for an additive manufacturing printer based on material extrusion. J Adv Manuf Technol 2019;105:2403–14.
[34] Augustine R, Hasan A, Patan NK, Dalvi YB, Varghese R, Antony A, Unni RN, Sandhyarani N, Moustafa AEA. Cerium oxide nanoparticle incorporated electrospun poly(3-hydroxybutyrate-co-3-hydroxyvalerate) membranes for diabetic wound healing applications. ACS Biomater Sci Eng 2020;6:58–70.
[35] Patil S, Sandberg A, Heckert E, Self W, Seal S. Protein adsorption and cellular uptake of cerium oxide nanoparticles as a function of zeta potential. Biomaterials 2007;28:4600–7.
[36] Naganuma T, Traversa E. The effect of cerium valence states at cerium oxide nanoparticle surfaces on cell proliferation. Biomaterials 2014;35:4441–53.
[37] Bagus PS, Nelin CJ, Hrovat DA, Ilton ES. Covalent bonding in heavy metal oxides. J Chem Phys 2017;146:134706.
[38] Nelin CJ, Bagus PS, Ilton ES, Chambers SA, Kuhlenbeck H, Freund HJ. Relationships between complex core level spectra and materials properties. Int J Quantum Chem 2010;110:2752–64.
[39] Kuchma MH, Komanski CB, Colon J, Teblum A, Masunov AE, Alvarado B, Babu S, Seal S, Summy J, Baker CH. Phosphate ester hydrolysis of biologically relevant molecules by cerium oxide nanoparticles. Nanomedicine 2010;6:738–44.
[40] Singh S, Dosani T, Karakoti AS, Kumar A, Seal S, Self WT. A phosphate-dependent shift in redox state of cerium oxide nanoparticles and its effects on catalytic properties. Biomaterials 2011;32:6745–53.
[41] Wu Y, Lin X, Li J, Zhang C, Liu Y, Song L, Hao X, Lin F, Wang S, Dong T. Polylactic acid/cerium fluoride films: effects of cerium fluoride on mechanical properties, crystallinity, thermal behavior, and transparency. Materials 2021;14:4882.
[42] Xiao L, Wang B, Yang G, Gauthier M. Poly(lactic acid)-based biomaterials: synthesis, modification and applications. biomedical science, engineering and technology. D.N. Ghista. Biomedical science, engineering and technology. London: Intechopen; 2012. p. 247–82.
[43] Stratton S, Shelke NB, Hoshino K, Rudraiah S, Kumbar SG. Bioactive polymeric scaffolds for tissue engineering. Bioact Mater 2016;1:93–108.
[44] Shasteen C, Choy YB. Controlling degradation rate of poly(lactic acid) for its biomedical applications. Biomed Eng Lett 2011;1:e163.
[45] Denry I, Kuhn LT. Design and characterization of calcium phosphate ceramic scaffolds for bone tissue engineering. Dent Mater 2016;32:43–53.
[46] Kumar A, Mandal S, Barui S, Vasireddi R, Gbureck U, Gelinsky M, Basu B. Low temperature additive manufacturing of three dimensional scaffolds for bone-tissue engineering applications: processing related challenges and property assessment. Mater Sci Eng R Rep 2016;103:1–39.
[47] Rogowska-Tylman J, Locs J, Salma I, Woźniak B, Pilmane M, Zalite V, Wojnarowicz J, Kędzierska-Sar A, Chudoba T, Szlązak K, Chlanda A, Święszkowski W, Gedanken A, Łojkowski W. *In vivo* and *in vitro* study of a novel nanohydroxyapatite sonocoated scaffolds for enhanced bone regeneration. Mater Sci Eng C 2019;99:669–84.
[48] Hutmacher DW, Schantz JT, Lam CXF, Tan KC, Lim TC. State of the art and future directions of scaffold-based bone engineering from a biomaterials perspective. J Tissue Eng Regen Med 2007;1:245–60.
[49] Nilawar S, Chatterjee K. Surface decoration of redox-modulating nanoceria on 3d-printed tissue scaffolds promotes stem cell osteogenesis and attenuates bacterial colonization. Biomacromolecules 2022;23:226–39.
[50] Liu DD, Zhang JC, Zhang Q, Wang SX, Yang MS. TGF-β/BMP signaling pathway is involved in cerium promoted osteogenic differentiation of mesenchymal stem cells. J Cell Biochem 2013;114:1105–14.

[51] Hu M, Xiao F, Ke QF, Li Y, Chen XD, Guo YP. Cerium doped whitlockite nanohybrid scaffolds promote new bone regeneration via SMAD signaling pathway. Chem Eng J 2019;359:1–12.
[52] Li K, Shen Q, Xie Y, You M, Huang L, Zheng X. Incorporation of cerium oxide into hydroxyapatite coating regulates osteogenic activity of mesenchymal stem cell and macrophage polarization. J Biomater Appl 2017;31:1062–77.
[53] Ghayor C, Bhattacharya I, Guerrero J, Özcan M, Weber FE. 3D-printed HA-based scaffolds for bone regeneration: microporosity, osteoconduction and osteoclastic resorption. Materials 2022;15:1433.
[54] Podgórski R, Wojasiński M, Trepkowska-Mejer E, Ciach T. A simple and fast method for screening production of polymer-ceramic filaments for bone implant printing using commercial fused deposition modelling 3D printers. Biomater Adv 2023;146:213317.
[55] Cestari F, Petretta M, Yang Y, Motta A, Grigolo B, Sglavo VM. 3D printing of PCL/nano-hydroxyapatite scaffolds derived from biogenic sources for bone tissue engineering. Sustain Mater Technol 2021;29:e00318.
[56] Wei J, Yan Y, Gao J, Li Y, Wang R, Wang J, Zou Q, Zuo Y, Zhu M, Li J. 3D-printed hydroxyapatite microspheres reinforced PLGA scaffolds for bone regeneration. Biomater Adv 2022;133:112618.
[57] Manzoor F, Golbang A, Jindal S, Dixon D, McIlhagger A, Harkin-Jones E, Crawford D, Mancuso E. 3D printed PEEK/HA composites for bone tissue engineering applications: Effect of material formulation on mechanical performance and bioactive potential. J Mech Behav Biomed Mater 2021;121:104601.